

Harnessing the power of complex light propagation in multimode fibers for spatially resolved sensing

Darcy L. Smith^{1,2,3,**}, Linh V. Nguyen^{3,4,**}, Mohammad I. Reja^{1,3}, Erik P. Schartner¹, Heike Ebendorff-Heidepriem¹, David J. Ottaway^{1,2,*} and Stephen C. Warren-Smith^{3,4,*}

¹ *Institute for Photonics and Advanced Sensing and The School of Physics, Chemistry and Earth Sciences, The University of Adelaide, Adelaide, SA 5005, Australia*

² *Australian Research Council Centre of Excellence for Gravitational Wave Discovery (OzGrav)*

³ *Future Industries Institute, University of South Australia, Mawson Lakes, SA 5095, Australia*

⁴ *Laser Physics and Photonics Devices Laboratory, University of South Australia, Mawson Lakes, SA 5095, Australia*

* Correspondence: Stephen C. Warren-Smith (stephen.warren-smith@unisa.edu.au) or David J. Ottaway (david.ottaway@adelaide.edu.au)

** *These authors contributed equally to this work*

Abstract

The propagation of coherent light in multimode optical fibers results in complex light patterns known as speckle. This effect has historically made understanding and controlling the light transport in these fibers extremely difficult, with successes such as imaging still being restricted to special cases. This complexity can also be a powerful tool for sensing environmental parameters, as small perturbations lead to significant changes in the output of the fiber. Until now, the ability to use speckle patterns for longitudinally resolved sensing has remained unclear, with previous studies limited to the classification of fiber bending positions and thus lacking quantification. In this paper, we demonstrate that random longitudinal variations which are usually regarded as a significantly detrimental property are crucial to achieving spatially resolved measurements. The mode coupling induced by such variations break the longitudinal symmetry of the fiber causing the fiber's output to become dependent on the longitudinal position of such a perturbation. In this work we use machine learning to quantitatively extract this spatial information and compare three fiber types with dramatically different mode coupling and sensitivity characteristics. We show that sapphire crystal fiber, which supports a high degree of mode coupling due to significant diameter inhomogeneities, provides the greatest accuracy. These findings have far-reaching implications for the broader optics and photonics research community in the study of complex light propagation and offers exciting opportunities for the development of new and innovative sensing technologies.

Introduction

The propagation of light through complex media results in complicated behavior that has traditionally been seen as a hindrance to optical systems, which should be avoided or compensated for. Precision instruments, such as gravitational-wave detectors, require ultrahigh vacuums to avoid material interactions¹. When propagation through media cannot be avoided, such as ground-based astronomy, complex adaptive optics are used to correct for the distortions². Sometimes, light propagation through complex media can also be used to advantage. Random lasers are a striking example where lasing is achieved without a defined resonator^{3,4} to produce high brightness but low coherence light for speckle-free imaging⁵.

Waveguides can lead to complex light propagation even in the absence of material inhomogeneity via their discrete transverse modes whose phase relationship varies with propagation. The resulting output field is inherently deterministic but highly complex in practice, due to interference between the many guided modes, interaction with the environment, and mode coupling. Recently, there has been significant interest in

understanding and exploiting the transmission of light through multi-mode optical fiber (MMF), due to their inherent ability to transport a greater amount of information than single mode fiber (SMF)⁶. A field that has particularly leveraged the power of MMF is imaging, with applications such as endoscopy^{7,8} and fluorescence imaging⁹. MMFs have also been utilized for applications such as high-resolution spectrometry^{10,11}, laser pulse characterisation¹², fiber amplifier beam shaping¹³, and control of nonlinear light generation¹⁴. In these cases, the fiber and its environment are held static, and a map between the fiber's input and output is built.

Optical fiber sensing can be considered the inverse procedure; the optical input is fixed, while environmental perturbations on the optical fiber cause measurable changes at the output. Possible perturbations include temperature, strain, pressure, or even biochemical interactions, all of which can induce optical path length changes in the optical fiber¹⁵. When coherent light is coupled into a MMF, these environmental perturbations lead to complex changes in the transverse spatial intensity output (specklegram)¹⁶. Typically, the specklegram is analyzed by comparing the measured output to a reference image using correlation techniques¹⁷⁻¹⁹ or machine learning^{20,21}. We have recently shown that the combination of deep learning with MMF interferometry allows for accurate sensing even in the presence of significant environmental noise²². In these cases, the sensor integrates the measurand along the length of the fiber, effectively yielding a single longitudinal measurement point.

The true power of optical fibers for sensing is multi-point or distributed sensing²³⁻²⁵. This is generally achieved in single mode fiber (SMF) using time or frequency domain interrogation methods, such as Brillouin scattering based distributed fiber sensing^{26,27}. The following question then arises – is it possible to perform spatially resolved sensing directly using the sensitive, but complex, MMF interference? Recent reports indicate this is indeed possible, with deep learning being applied to extract spatial information from an MMF's output for sensing²⁸⁻³⁰. Such demonstrations have shown the ability to classify the location of a perturbation, but were restricted to qualitative analysis. Nevertheless, important insights can be drawn from such work, like that deep neural network (DNN) accuracy increases for sensing locations along the fiber which are closer to the light interrogation apparatus²⁹, and that a ring core fiber supporting several weakly-coupled mode groups could achieve greater accuracy with less training data compared to conventional graded-index multi-mode fiber³⁰.

In this paper, to the best of our knowledge, we demonstrate the first quantitative, interference-based, multi-point MMF sensor. This is demonstrated by accurately measuring temperature at ten spatially separated locations. We compare the effectiveness of three distinctly different MMF architectures: a graded-index fiber, a microstructured optical fiber,

and a sapphire crystal optical fiber. Using deep learning, the spatially encoded sensing information is resolved with high accuracy. Our results lead to the new understanding of MMF sensing that longitudinal inhomogeneities are of benefit for spatially resolved sensing. The sapphire fiber displays better longitudinal sensing resolution capabilities than the two other fibers, due to having significant diameter inhomogeneities along its length formed by the crystal fabrication process. This allows spatial information to be more rigorously encoded in the complex interferometric output through mode coupling. This approach opens a new pathway for distributed fiber sensing directly with the raw, complex interference pattern output of MMFs, significantly simplifying hardware requirements and broadening the range of fiber materials that can be deployed.

Results

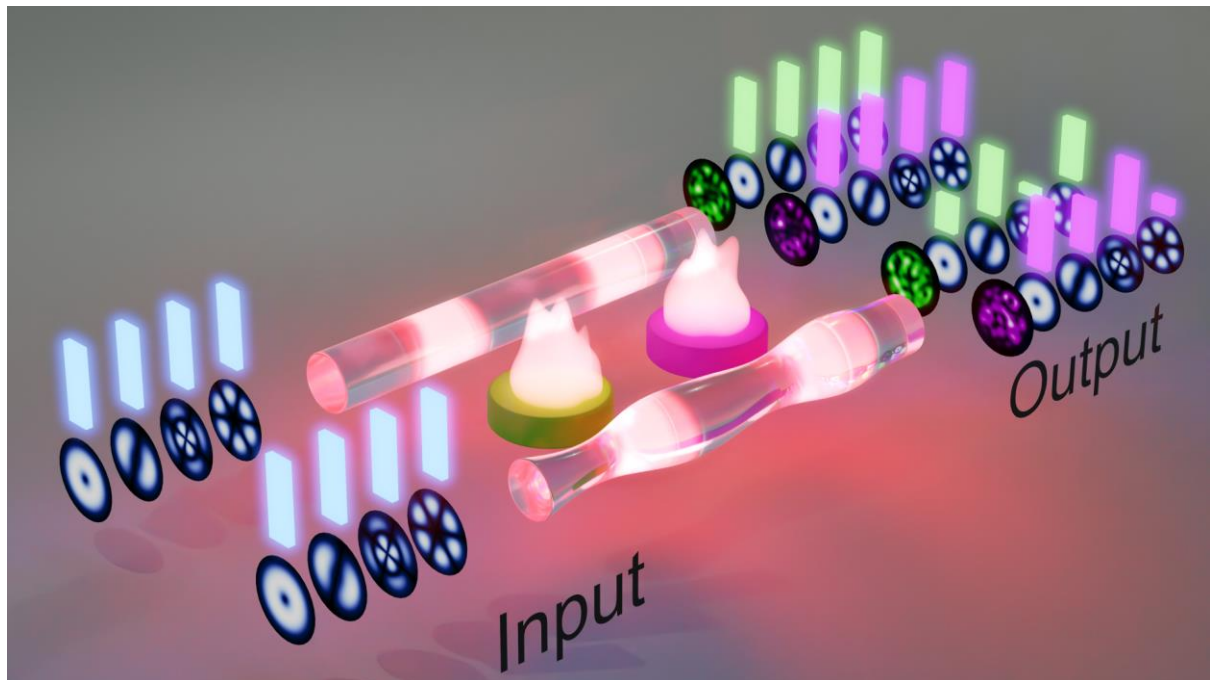


Fig. 1: Concept of spatially resolved sensing enabled by distributed mode mixing: comparison between a longitudinally invariant fiber and a fiber with diameter variations. The light within a multimode optical fiber consists of a superposition of eigenmodes, each carrying a portion of the total power propagating in the fiber. A perturbation on the fiber will induce mode-dependent phase changes, which will be reflected in a change in the output of the fiber, whether this is the spatial interference pattern (specklegram) shown in the figure, or the wavelength domain interference spectrum used in this work. In this figure, two different longitudinal positions that experience identical perturbations are shown in green and purple, resulting in the corresponding color-coded modal amplitudes. For a perfectly longitudinally invariant fiber (left), the position of this perturbation will be indistinguishable at the output, as the modes will travel through the fiber free from coupling and power redistribution, thus rendering the effect of mode-dependent optical path length changes position independent. In the case of an optical fiber with longitudinal variations (right), mode coupling leads to modal power redistribution, rendering the effect of these path length changes position-dependent, hence allowing for longitudinally resolved sensing.

Concept

In this paper, we investigate both theoretically and experimentally the ability to perform multi-point fiber sensing directly with the multimode interference in an MMF. We show through the

use of a MMF mode coupling theory framework³¹, which considers multimode light propagation, mode coupling and fiber gain/loss, that mode coupling in an MMF gives its output longitudinal spatial resolution (along the fiber axis). It is concluded that a longitudinally symmetric fiber free from mode coupling has no ability to longitudinally resolve perturbations, and that this symmetry must be broken in order to resolve the position of such perturbations. This concept is shown graphically in Fig. 1.

In this framework, the electric field propagating through an MMF with N orthogonal transverse eigenmodes can be expressed as:

$$\mathbf{E}(x, y, z) = \sum_{j=1}^N A_j(z) \hat{\mathbf{e}}_j(x, y), \quad (1)$$

where $\hat{\mathbf{e}}_j$ denotes the electric field profile of the j^{th} orthonormal transverse eigenmode, and A_j contains its amplitude and phase. Assuming fixed eigenmodes, the light can be described fully by the vector \mathbf{A} ,

$$\mathbf{A} = (A_1(z), \dots, A_N(z)). \quad (2)$$

Propagation of this field through an optical system can be expressed as:

$$\mathbf{A}^{(out)} = \mathbf{M}^{(t)} \mathbf{A}^{(in)}, \quad (3)$$

where $\mathbf{M}^{(t)}$ is an $N \times N$ matrix, termed the ‘propagation matrix’ of the system, which includes the effects of phase accumulation, mode dependent gain/loss, and mode coupling.

The propagation of the light through multimode fiber can be modelled by dividing the fiber into K adjacent sections, the k^{th} section having length $L^{(k)}$. The k^{th} propagation matrix can be decomposed as:

$$\mathbf{M}^{(k)} = \mathbf{V}^{(k)} \mathbf{\Lambda}^{(k)} \mathbf{U}^{(k)*}, \quad (4)$$

where $\mathbf{\Lambda}^{(k)}$ represents coupling-free propagation, given by

$$\mathbf{\Lambda}^{(k)} = \begin{bmatrix} \exp\left(\frac{1}{2}g_1^{(k)} - i\phi_1^{(k)}\right) & & 0 \\ & \ddots & \\ 0 & & \exp\left(\frac{1}{2}g_N^{(k)} - i\phi_N^{(k)}\right) \end{bmatrix}, \quad (5)$$

and U and V denote the input and output coupling matrices to and from this section, respectively. The real part of the exponentials in Eq. (5) describe mode-dependent loss or gain, where $g_j^{(k)}$ is the gain coefficient of the j^{th} mode in the k^{th} section of fiber. The imaginary part, $i\phi_j^{(k)}$, where $\phi_j^{(k)} = \beta_j L^{(k)}$ and β_j denotes the propagation constant of the j^{th} mode, describes the accumulated phase of the j^{th} mode as it passes through the k^{th} section of fiber. This is mode-dependent due to effects such as modal dispersion and mode-dependent chromatic dispersion.

Propagation of light through the entire fiber can be represented by the cascade of K propagation matrices in Eq. (6).

$$M^{(t)} = M^{(K)} M^{(K-1)} \dots M^{(k)} \dots M^{(2)} M^{(1)}. \quad (6)$$

Now consider that the k^{th} section of fiber experiences a perturbation, inducing mode dependent optical path length changes and hence phase changes in the field in this section. Such a perturbation can be modelled by a diagonal perturbation matrix $\tilde{\Lambda}$ (Eq. (7)), which describes the change in optical path length that each mode experiences.

$$\tilde{\Lambda} = \begin{bmatrix} \exp(-i\Delta\phi_1) & & 0 \\ & \ddots & \\ 0 & & \exp(-i\Delta\phi_N) \end{bmatrix} \quad (7)$$

Hence, the total propagation matrix in the presence of this perturbation is given by Eq. (8).

$$M^{(t)} = M^{(K)} M^{(K-1)} \dots V^{(k)} \tilde{\Lambda} \Lambda^{(k)} U^{(k)*} \dots M^{(2)} M^{(1)}. \quad (8)$$

The matrix multiplication $U^{(k+1)*} V^{(k)}$, represents projection of the field from the modal basis in the k^{th} section to the $(k+1)^{th}$ section, i.e., mode coupling. If the modal bases are identical, this term reduces to the identity matrix, and no mode coupling occurs. In the case of mode coupling between the sections, off-diagonal terms will be present.

Consider now a longitudinally symmetric MMF which experiences no mode coupling. $M^{(t)}$ will be the product of diagonal uncoupled propagation matrices and products of input and output coupling matrices projecting the fiber's modal basis onto itself, producing the identity matrix. Hence, $M^{(t)}$ will itself be diagonal, with the j^{th} diagonal element representing the sum of the gain/loss and phase accumulated by the j^{th} mode. The inclusion of a perturbation, $\tilde{\Lambda}$, will add its mode-dependent phase changes to this sum, regardless of

where it occurs along the fiber. Hence, such a longitudinally symmetric fiber possesses no spatially resolved sensing capabilities.

Now consider a MMF with longitudinal variance, and hence coupling between modal bases existing in different sections of the fiber. The total propagation matrix $M^{(t)}$ will now no longer be diagonal, as off-diagonal terms representing the coupling of power between modes will be present. As such, it will also be dependent on the order of multiplication of its constituent propagation matrices. Hence in the presence of optical path length changes due to a perturbation, the fiber's output will be dependent on the position of this perturbation along the fiber.

If we compare the case of fiber that supports either weak or strong coupling, the length at which the same degree of mode coupling is achieved will be relatively shorter for the strong mode coupling case. This can be considered as the length for which adjacent propagation matrices have the same degree of commutation. Therefore, strong mode coupling fibers are expected to support finer degrees of spatial resolution for sensing, given the same instrumentation and environmental perturbations.

The spatially resolved sensing information is, however, encoded in the fiber's output in a complex and non-trivial way. We have previously shown that deep learning proves an effective method for extracting single-point sensing information from a complex MMF output²². In this work, deep learning is used as a tool for extracting distributed sensing information from this output.

Experimental design

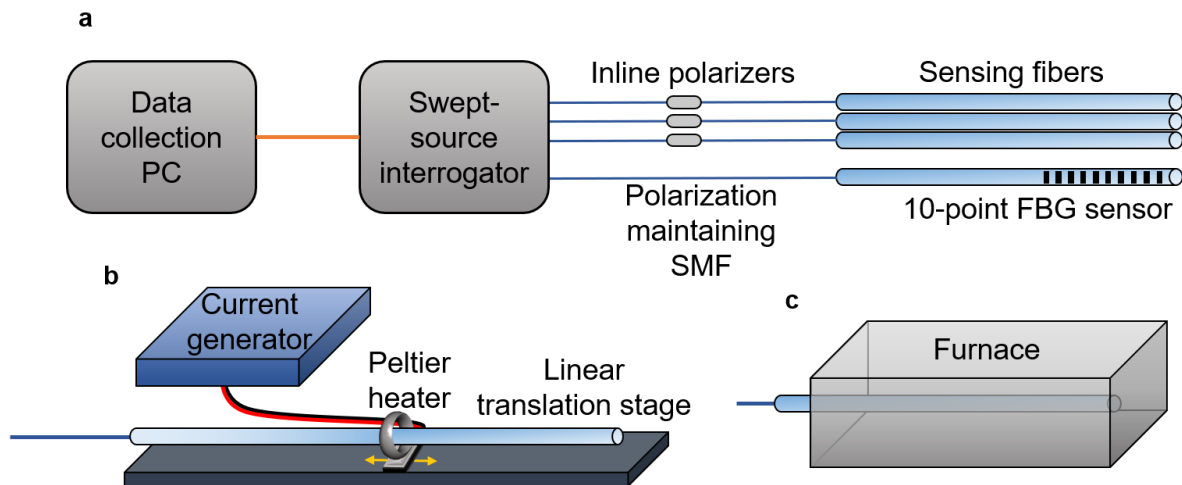


Fig. 2: Experimental setup. **a** Overview of the setup used to collect wavelength intensity spectra from the fibers under different temperature distributions. A swept-source interrogator from 1460-1620 nm recorded spectra produced by the reflected light from the cleaved end facets of the MMF coupled back into SMF. Polarization maintaining SMF was used in conjunction with inline polarizers so as to prevent polarization mode coupling within the SMF. **b** The experimental setup for the localized heating experiment. The fibers were subjected to a local heating perturbation through means of an aluminum block attached to a Peltier heater, translated via a linear translation stage. **c** The experimental setup for the furnace heating experiment. The fibers were subjected to

various temperature distributions by being placed in a furnace, with the distributions being varied by manually translating the fibers relative to the furnace.

Two experiments were performed to experimentally test the concepts presented using three multimode optical fibers: a sapphire optical fiber (80 μm diameter, Micromaterials), an in-house fabricated suspended-core fiber (SCF) (10 μm core diameter)³², and a graded-index (GRIN) fiber (OM1, FS). An overview of the method used to collect wavelength interference spectra from these fibers is shown in Fig. 2a. All three fibers were spliced to polarization maintaining SMF which converted the MMF speckle information into an interference spectrum (more details in the Supplementary Information). The technical characteristics of the three fibers are compared in Table S1, but their relevant characteristics for the purposes of this paper are as follows. As the sapphire fiber is fabricated via crystal growth, rather than by preform fabrication as would be the case with conventional glass optical fibers, it has significant longitudinal diameter variations (see Fig. S1 and S2), leading to strong mode coupling along its length. The SCF is designed for temperature sensing, supporting the propagation of modes with relatively large differences in thermo-optic response compared to solid fibers³³. In contrast to the sapphire fiber, both the SCF and GRIN fibers are designed and fabricated with the aim of producing a consistent diameter.

The first experiment, represented in Fig. 2b, subjected the fibers to a series of spatially resolved local heat perturbations. In this case the perturbation took the form of a heater with constant temperature but translated longitudinally along the fibers. The correlation of the MMF output compared to a reference spectrum was then measured to determine the degree to which the perturbation location induced differing outputs. This experiment gives a relative comparison of the fibers' mode coupling lengths, and hence the spatial resolution of distributed sensing information accrued by the light propagating through them.

The second experiment, represented in Fig. 2c, subjected the fibers to a range of different spatial temperature distributions generated by a furnace, and used two DNNs of differing capacity to test how retrievable any spatially resolved sensing information was from their outputs. The two models tested were a multi-layer perceptron network (MLP) with four hidden layers and a linear regressor with no hidden layers. The MLP was chosen as a relatively powerful model for this task, demonstrating how accurate the temperature distributions can be predicted using deep learning. The linear regressor was chosen to demonstrate a level of computational ability at which a clear difference of accuracy was apparent across the models trained on each fiber's spectra. Fig. S3 and S4 give schematic representations of the models and the loss history for the training performed in this work respectively. Table S2 and S3 give details regarding the model architectures.

Localized heating: correlation analysis

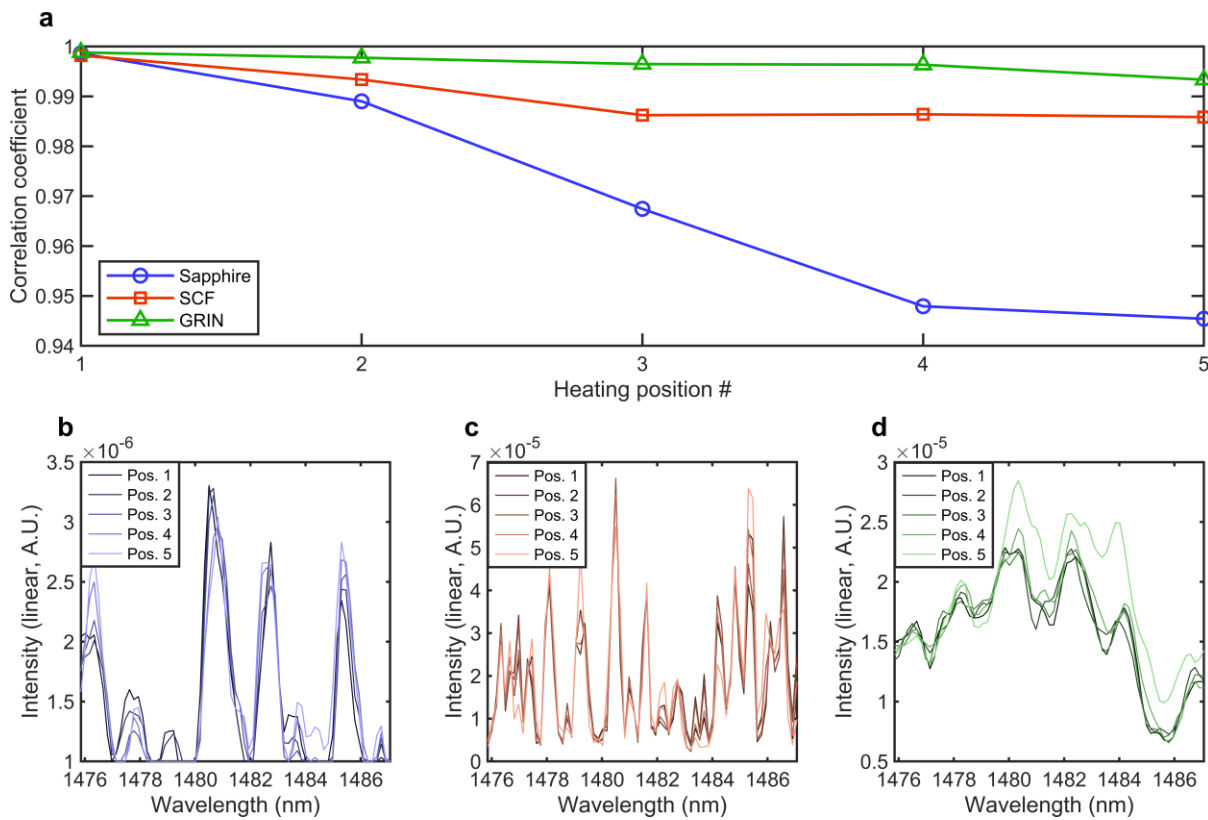


Fig. 3: Results from the localized heating experiment. **a** The average correlation coefficient of spectra collected during each 30 min heating position against the reference spectrum (the first spectrum collected from heating position #1). **b-d** Example spectra over a zoomed in wavelength range from all five heating positions for the sapphire, suspended-core, and graded-index fiber, respectively.

The first set of results are from the localized heating experiment. Approximately 1 700 wavelength spectra were collected from each position before moving to the next, for a total of five equidistant heater positions along the fibers' length. The thermal distribution resulting from each heating position is shown in Fig. **S7**. The correlation coefficient for each spectrum was calculated against a reference spectrum from the first temperature profile, and the average correlation coefficient value (Eq. (9)) for each position was calculated and are displayed in Fig. **3a**. A lower correlation coefficient for a spectrum indicates relatively larger decorrelation from the reference spectrum. Hence unique correlation values for different heating locations, continuously decreasing from the reference spectrum, indicates longitudinal resolution in the fiber output. The correlation coefficient for every collected spectrum as a full function of time is shown in Fig. **S9**.

Results of how the spectra from each fiber change due to the position of the thermal perturbation applied to them are shown in Fig. **3b-d** for the sapphire, suspended-core, and graded-index fibers, respectively. An example spectrum from each heating position for each fiber is displayed. The spectra are zoomed in to a ~ 10 nm range, so as to display the spectral features more clearly.

The results indicate that the recorded spectra from each fiber have different dependencies on the position of the thermal perturbation. It is clearly shown that the spectrum of the sapphire fiber is more dependent on the position of the heater, as indicated by the correlation coefficient continuously decreasing with heater translation. The spectra collected from the SCF and GRIN fiber do not display this dependence as clearly, with the respective correlation coefficients staying closer to unity over the whole range of the fiber lengths. As argued in the theory, weak mode coupling implies that the effect of a perturbation on the fiber's output will only be weakly dependent on the position of the perturbation, leading to similar outputs for the different temperature profiles. In contrast, strong location dependency indicates strong mode coupling, hence the correlation coefficient decreases quicker as the location of the perturbation is shifted from its original location.

With reference to the specific fibers used, it is the significant longitudinal variance of the sapphire fiber, shown in Fig. **S2**, which induces mode coupling continuously along its length, hence enhancing the spatial resolution of sensing information in its output. The SCF and GRIN fibers are expected to exhibit much less mode coupling due to being drawn with minimal longitudinal variations, and in the absence of significant mechanical perturbations, having no other method by which couple light between modes in our experiment. We note that the change in correlation for the SCF is greater than the GRIN, which is attributed to its higher overall temperature sensitivity and thus sensitivity to subtle changes in the temperature distribution as the heater is moved.

Distributed heating: deep learning analysis

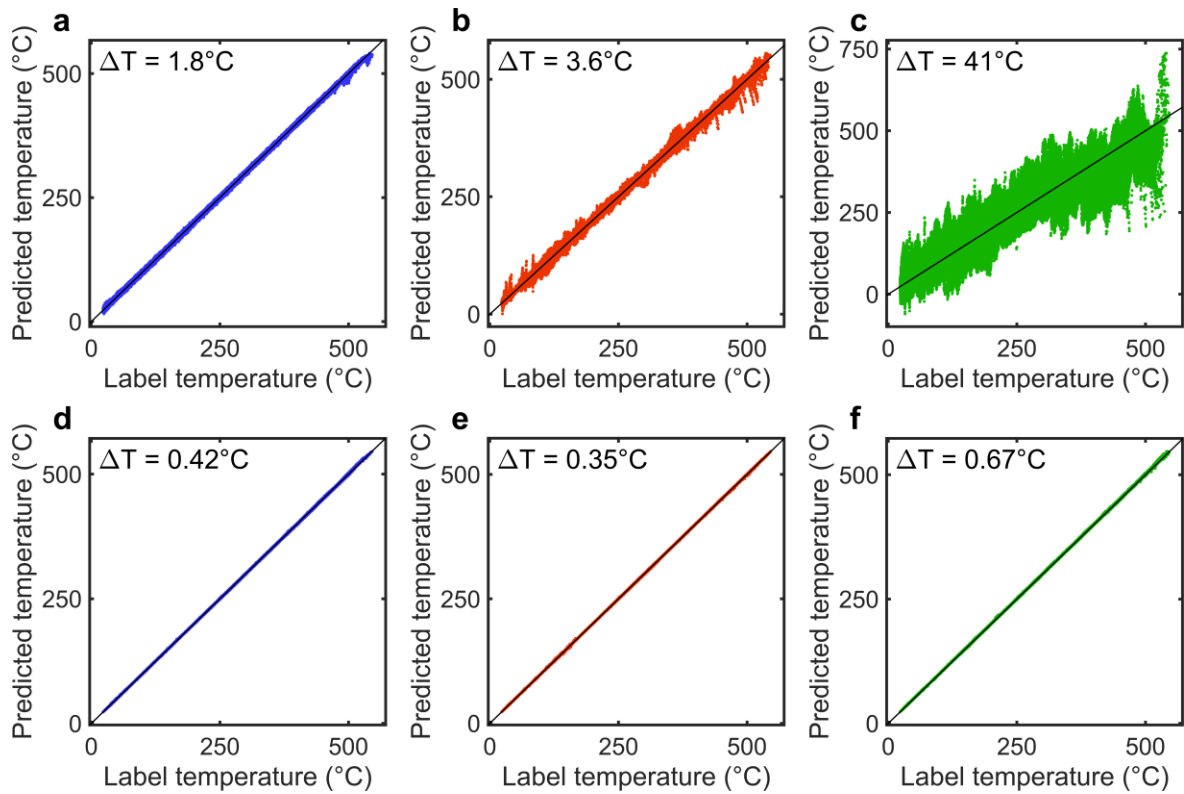


Fig. 4: Results from the distributed heating experiment. Predictions made by the DNNs on the 10-point temperature distributions from the wavelength interference spectra. The DNNs had an output layer of 10 nodes to make the 10 longitudinally resolved sensing predictions simultaneously, but all predictions from each given DNN have been combined to produce each plot. Predictions were made on a test set of spectra, which were kept aside during all preliminary model training, and only used to produce the figures seen in this paper. **a-c** Predictions made by the linear regressor. **d-f** Predictions made by the MLP. **a** and **d** show the predictions from DNNs trained on sapphire spectra, **b** and **e** SCF spectra, and **c** and **f** GRIN fiber spectra.

The results from the second experiment show the temperature predictions made by the DNNs trained on wavelength spectra from each fiber under different temperature distributions produced by a furnace (Fig. 2c). Fig. 4a-c shows the predictions made by the linear regressor, while Fig. 4d-f shows those made by the MLP. The associated RMS error for each set of predictions is displayed. The temperature labels were collected by the 10-point FBG sensor (example temperature distributions are shown in Fig. S8). The DNNs had 10 nodes in their output layer, hence trained to predict 10-point temperature distributions. For simplicity, the predictions on all 10 sensing points (47 600 test spectra) are included in each plot of Fig. 4. The error as a function of each sensing point is shown in Fig. S10.

The multi-layer perceptron (MLP) is able to predict the 10-point temperature distribution under which the unseen test set of spectra were collected with high accuracy for all three fibers. As one would expect, the linear regressor performs less accurately. Given its heavily reduced number of trainable parameters compared to the MLP, it is less successful at finding the map between a fiber's distributed temperature environment and its wavelength intensity spectra.

As discussed in the Concept section, mode coupling should be required to perform spatially resolved fiber sensing with an otherwise unaltered fiber. This result that the MLP performs accurately when trained on spectra from either of the three fibers suggests that the level of inherent mode coupling present in the two otherwise longitudinally invariant fibers is sufficient to encode spatially resolved sensing information in the spectra, at least to the 15 mm resolution measured in this experiment. This may be induced by the sensing parameter itself, as temperature variations lead to refractive index modulations.

The results from the linear regressor show more clearly a quantitative difference in DNN performance. The model achieves an RMS error of 1.8°C when trained on spectra from the sapphire fiber, 3.6°C for the SCF spectra, and 41°C for the GRIN fiber spectra. The lower-capacity linear model used amplifies the difference in ability for the model to extract longitudinally resolved sensing information from the spectra from the different models. In agreement with our theoretical framework and the correlation analysis results, the sapphire fiber shows better sensitivity to the position of a perturbation, or in the more general case, the spatial distribution of a perturbation.

Discussion

The results presented support the concept that deep learning can be used to extract distributed sensing information from the output of a MMF. The presence of mode coupling in the MMF facilitates stronger encoding of this information in its output, leading to better spatial resolution along its length.

The results from the localized heating experiment are in agreement with the theory we have presented. The mode coupling lengths associated with the SCF and GRIN fibers are considerably longer than the sapphire fiber given the greater longitudinal invariance of these two fibers. Consequently, the output of the sapphire fiber in the presence of a localized perturbation will be more positionally dependent than that of the SCF and GRIN fibers. This is reflected in Fig. 3a, as the sapphire spectrum decorrelates from the reference spectrum quicker and more strongly than the SCF and GRIN fibers as the perturbation is translated beyond its coupling-free length.

The results from the furnace heating experiment are in further support of the distributed sensing capabilities that the sapphire possesses due to its inherent mode coupling. They also suggest that deep learning is well suited to the task of decoding spatially resolved sensing information in the output of an MMF, given the MLP's success with spectra from all three fibers, even those of the SCF and GRIN fibers. This can be attributed to the small amount of unavoidable mode coupling that these fibers possess, as well as the nature of the temperature distributions achieved by the furnace, and how these were far from arbitrary. As

such, sufficient distributed temperature information is encoded in the spectra of all three fibers for the DNN to learn.

The performance of the linear regressor however gives more insight into how clearly each fiber encodes distributed sensing information in their outputs. This low-capacity model is able to extract this information from the sapphire fiber spectra to an RMS error of 1.8°C , half that of the SCF, and 20 times less than that of the GRIN fiber. This is aided by the mode coupling which occurs along the sapphire fiber's length, encoding longitudinally resolved sensing information in its output, which can be more efficiently extracted through deep learning techniques.

Materials and methods

Fiber preparation and data collection

Four fibers were used to collect data in the experiment; three sensing fibers and an FBG sensor array to collect temperature labels. The three sensing fibers used were sapphire crystal optical fiber (Micromaterials), in-house fabricated silica suspended core fiber³² and silica graded-index fiber (FS). The cross-section and selected properties of these fibers are displayed in Table **S1**. Each fiber was prepared by splicing a polarization-maintaining SMF to its end, with the SMF connected at the other end to the interrogator via an FC/LC connection. To facilitate a reflection signal, the distal end of each fiber was prepared flat. The SCF and GRIN fibers were cleaved using the standard crack-cleave method while the sapphire crystal fiber was polished. Fig. **S6** gives a schematic of the sensors.

A 10-point FBG sensor was deployed alongside the three sensing fibers to collect temperature labels for deep learning and characterize the temperature distributions the fibers were subjected to. This FBG sensor consisted of 10 femtosecond laser ablation written gratings inscribed in a suspended-core microstructured optical fiber³⁴⁻³⁶. The ten FBGs were spaced 15 mm apart, thus performing temperature sensing over a 135 mm length.

The general method of collecting wavelength spectra from the fibers is shown in Fig. **2a**. After reflecting from the sensing fibers' end facets, the light coupled into the polarization-maintaining SMF, thus projecting their superposition of modes onto a single mode. The power propagating in this single mode for a range of wavelengths comprised the wavelength intensity spectrum. This spectrum was interrogated by a 1460-1620 nm Hyperion si155 (Luna Technologies) swept source interrogator. Inline fiber polarizers were used to restrict the light to a single polarization axis and prevent coupling between polarization modes. Each

fiber was packaged within an Inconel tube to protect it from contaminants at high temperature.

Examples of spectra collected from the interrogator are shown in Fig. S5a-c. Due to the difficulty of splicing the sapphire fiber to the silica SMF, the wavelength spectra collected from the sapphire fiber contained a strong noise envelope, originating from the back-reflection of the sapphire-SMF splice. Hence, post-processing was performed identically on all spectra to remove the five lowest frequency components from the fast Fourier transforms of the spectra, thus removing this noise envelope and maximizing the signal to noise ratio of the sapphire fiber's interference peaks. The modified spectra are shown in Fig. S5d-f. These spectra were used for training the DNNs.

Localized heating experiment

In this experiment, the fibers were subjected to a localized source of heat, in the form of radiative and convective heat from an aluminum ring, heated by a Peltier heater. This heating apparatus was fixed to a linear translation stage (Optosigma OSMS33-(X)), controlled by a PC in order to facilitate the translation of this localized heat profile along the longitudinal axis of the fibers. Five successive, equidistant heating positions along the length of the fibers were performed, beginning at the SMF-splice end of the fibers. Spectra were recorded at a rate of 1 Hz, with the heater in each position for 30 min. Thermal equilibrium was reached after approximately 5 min each time the heater was moved. The spectra collected while the sensors reached thermal equilibrium did not contribute to Fig. 3a.

The changes experienced by each fiber's wavelength intensity spectra $I(\lambda)$ were quantified using the zero-normalised cross correlation function (ZNCC), defined by

$$Z(I(\lambda)) = \frac{\sum_{\lambda} (I_0 - \bar{I}_0)(I - \bar{I})}{[\sum_{\lambda} (I_0 - \bar{I}_0)^2 \sum_{\lambda} (I - \bar{I})^2]^{\frac{1}{2}}}, \quad (9)$$

where $I_0(\lambda)$ denotes a reference intensity spectrum and the bar denotes the average intensity of the relevant spectrum.

Furnace heating experiment

In this experiment, the wavelength spectra from the four fibers were collected in nine 24 hour sets, each with the fibers side by side in a different position relative to the furnace. For each set, spectra were collected at a rate of 1 Hz over a period of 20 h as the furnace was allowed to cool from 500°C to 50°C. By collecting data with this method, the fibers were exposed to a variety of temperature distributions, as both the fiber position and furnace temperature were variables affecting the distribution experienced by the fibers, as represented in Fig. S8.

These spectra, along with the 10-point temperature data, were used in training the deep neural networks described below.

Deep learning

Two neural networks were employed in this work; a multi-layer perceptron model³⁷ with four hidden layers and 672 842 trainable parameters, and a linear regressor with 9 760 trainable parameters. The linear regressor learns an output which is simply a linear combination of the input values. Summaries of the model architectures are displayed in Table **S2** and **S3**, and a schematic of the models is shown in Fig. **S3**. The input layer for both was the 975-point normalized wavelength intensity spectra and the output layer was the 10 temperature predictions. The rectified linear unit (ReLU) activation³⁸ was applied after each hidden layer in the MLP.

The complete dataset consisted of 476 000 spectra for each fiber. Following normalization as per an L2 normalization technique and preceding training, this set was shuffled and split into three groups: 80% for training, 10% for validation, and 10% for testing. The training set was used to train the model and the validation set used to test the prediction ability and monitor the performance of the model during preliminary training runs. The test set was kept aside and only used to make predictions using the final trained model.

The deep learning model began the training process with randomized parameters. Then, mini-batches of 64 spectra were randomly selected from the training set and passed through the model. The loss (cost function) of the model was calculated using the mean-squared-error (MSE) metric, and backpropagation performed to adjust the model towards one with a lower loss³⁹. This process was repeated with batches of 64 training samples, until all samples had been used. This concluded one epoch of training. Training was performed for 150 epochs, with the end-of-epoch model exhibiting the lowest loss kept as the final model. Plots of the loss history are shown in Fig. **S4**.

Acknowledgements

Stephen Warren-Smith is supported by an Australian Research Council (ARC) Future Fellowship (FT200100154). Md. Istiaque Reja is supported by Australian Government Research Training Program Scholarship. This work was performed, in part, at the Optofab node of the Australian National Fabrication Facility utilizing Commonwealth and South Australian State Government funding.

Author contributions

D.L.S., L.V.N., S.C.W-S. and D.J.O. conceptualized the idea, designed the experiments, interpreted the results and contributed to the writing and editing of the manuscript. D.L.S. constructed the experiments and recorded data. H.E-H. and E.P.S. designed and contributed to the fabrication of the SCF. D.L.S. and M.I.R. worked with the fibers and fabricated the sensors. D.L.S. performed the machine learning with guidance from L.V.N.

Conflict of interest

The authors declare no competing interests.

References

- 1 Ligo Scientific Collaboration *et al.* Observation of Gravitational Waves from a Binary Black Hole Merger. *Physical Review Letters* **116**, 061102, doi:10.1103/PhysRevLett.116.061102 (2016).
- 2 Hippler, S. Adaptive Optics for Extremely Large Telescopes. *Journal of Astronomical Instrumentation* **08**, 1950001, doi:10.1142/S2251171719500016 (2018).
- 3 Cao, H. *et al.* Random Laser Action in Semiconductor Powder. *Physical Review Letters* **82**, 2278-2281, doi:10.1103/PhysRevLett.82.2278 (1999).
- 4 Wiersma, D. S. & Lagendijk, A. Light diffusion with gain and random lasers. *Physical Review E* **54**, 4256-4265, doi:10.1103/PhysRevE.54.4256 (1996).
- 5 Redding, B., Choma, M. A. & Cao, H. Speckle-free laser imaging using random laser illumination. *Nature Photonics* **6**, 355-359, doi:10.1038/nphoton.2012.90 (2012).
- 6 Mahalati, R. N., Gu, R. Y. & Kahn, J. M. Resolution limits for imaging through multi-mode fiber. *Optics Express* **21**, 1656-1668, doi:10.1364/OE.21.001656 (2013).
- 7 Turtaev, S. *et al.* High-fidelity multimode fibre-based endoscopy for deep brain in vivo imaging. *Light: Science & Applications* **7**, 92, doi:10.1038/s41377-018-0094-x (2018).
- 8 Leite, I. T., Turtaev, S., Boonzajer Flaes, D. E. & Čižmár, T. Observing distant objects with a multimode fiber-based holographic endoscope. *APL Photonics* **6**, 036112, doi:10.1063/5.0038367 (2021).
- 9 Čižmár, T. & Dholakia, K. Exploiting multimode waveguides for pure fibre-based imaging. *Nature Communications* **3**, 1027, doi:10.1038/ncomms2024 (2012).
- 10 Redding, B., Alam, M., Seifert, M. & Cao, H. High-resolution and broadband all-fiber spectrometers. *Optica* **1**, 175-180, doi:10.1364/OPTICA.1.000175 (2014).
- 11 Redding, B. & Cao, H. Using a multimode fiber as a high-resolution, low-loss spectrometer. *Optics Letters* **37**, 3384-3386, doi:10.1364/OL.37.003384 (2012).
- 12 Xiong, W. *et al.* Deep learning of ultrafast pulses with a multimode fiber. *APL Photonics* **5**, 096106, doi:10.1063/5.0007037 (2020).
- 13 Florentin, R. *et al.* Shaping the light amplified in a multimode fiber. *Light: Science & Applications* **6**, e16208-e16208, doi:10.1038/lsa.2016.208 (2017).
- 14 Tzang, O., Caravaca-Aguirre, A. M., Wagner, K. & Piestun, R. Adaptive wavefront shaping for controlling nonlinear multimode interactions in optical fibres. *Nature Photonics* **12**, 368-374, doi:10.1038/s41566-018-0167-7 (2018).
- 15 Grattan, K. T. V., Grattan, L. S. & Meggitt, B. T. *Optical Fiber Sensor Technology: Fundamentals*. (Springer New York, NY, 2000).
- 16 Leal-Junior, A. G., Frizera, A., Marques, C. & Pontes, M. J. Optical Fiber Specklegram Sensors for Mechanical Measurements: A Review. *IEEE Sensors Journal* **20**, 569-576, doi:10.1109/JSEN.2019.2944906 (2020).

- 17 Cabral, T. D., Fujiwara, E., Warren-Smith, S. C., Ebendorff-Heidepriem, H. & Cordeiro, C. M. B. Multimode exposed core fiber specklegram sensor. *Optics Letters* **45**, 3212-3215, doi:10.1364/OL.391812 (2020).
- 18 Fujiwara, E., Marques dos Santos, M. F. & Suzuki, C. K. Optical fiber specklegram sensor analysis by speckle pattern division. *Applied Optics* **56**, 1585-1590, doi:10.1364/AO.56.001585 (2017).
- 19 Yu, F. T. S., Wen, M., Yin, S. & Uang, C.-M. Submicrometer displacement sensing using inner-product multimode fiber speckle fields. *Applied Optics* **32**, 4685-4689, doi:10.1364/AO.32.004685 (1993).
- 20 Smith, D. L. *et al.* Machine learning for sensing with a multimode exposed core fiber specklegram sensor. *Optics Express* **30**, 10443-10455, doi:10.1364/OE.443932 (2022).
- 21 Li, G. *et al.* Deep learning based optical curvature sensor through specklegram detection of multimode fiber. *Optics & Laser Technology* **149**, 107873, doi:10.1016/j.optlastec.2022.107873 (2022).
- 22 Nguyen, L. V., Nguyen, C. C., Carneiro, G., Ebendorff-Heidepriem, H. & Warren-Smith, S. C. Sensing in the presence of strong noise by deep learning of dynamic multimode fiber interference. *Photon. Res.* **9**, B109-B118, doi:10.1364/PRJ.415902 (2021).
- 23 Lu, P. *et al.* Distributed optical fiber sensing: Review and perspective. *Applied Physics Reviews* **6**, 041302, doi:10.1063/1.5113955 (2019).
- 24 Motil, A., Bergman, A. & Tur, M. State of the art of Brillouin fiber-optic distributed sensing. *Optics & Laser Technology* **78**, 81-103, doi:10.1016/j.optlastec.2015.09.013 (2016).
- 25 Alan, R. Distributed optical-fibre sensing. *Measurement Science and Technology* **10**, R75, doi:10.1088/0957-0233/10/8/201 (1999).
- 26 Denisov, A., Soto, M. A. & Thévenaz, L. Going beyond 1000000 resolved points in a Brillouin distributed fiber sensor: theoretical analysis and experimental demonstration. *Light: Science & Applications* **5**, e16074-e16074, doi:10.1038/lsa.2016.74 (2016).
- 27 Horiguchi, T., Shimizu, K., Kurashima, T., Tateda, M. & Koyamada, Y. Development of a distributed sensing technique using Brillouin scattering. *Journal of Lightwave Technology* **13**, 1296-1302, doi:10.1109/50.400684 (1995).
- 28 Lu, S., Tan, Z., Li, G. & Yang, J. A Sensitized Plastic Fiber Sensor for Multi-Point Bending Measurement Based on Deep Learning. *IEEE Photonics Journal* **13**, 1-7, doi:10.1109/JPHOT.2021.3103566 (2021).
- 29 Cuevas, A. R., Fontana, M., Rodriguez-Cobo, L., Lomer, M. & López-Higuera, J. M. Machine Learning for Turning Optical Fiber Specklegram Sensor into a Spatially-Resolved Sensing System. Proof of Concept. *Journal of Lightwave Technology* **36**, 3733-3738, doi:10.1109/JLT.2018.2850801 (2018).
- 30 Wei, M. *et al.* Neural Network Based Perturbation-Location Fiber Specklegram Sensing System Towards Applications With Limited Number of Training Samples. *Journal of Lightwave Technology* **39**, 6315-6326, doi:10.1109/JLT.2021.3098345 (2021).
- 31 Ho, K.-P. & Kahn, J. Mode Coupling and its Impact on Spatially Multiplexed Systems. *Optical Fiber Telecommunications VIB: Systems and Networks: Sixth Edition*, doi:10.1016/B978-0-12-396960-6.00011-0 (2013).
- 32 Kostecki, R., Ebendorff-Heidepriem, H., Warren-Smith, S. C. & Monroe, T. M. Predicting the drawing conditions for Microstructured Optical Fiber fabrication. *Opt. Mater. Express* **4**, 29-40, doi:10.1364/OME.4.000029 (2014).
- 33 Nguyen, L. V., Warren-Smith, S. C., Ebendorff-Heidepriem, H. & Monroe, T. M. Interferometric high temperature sensor using suspended-core optical fibers. *Optics Express* **24**, 8967-8977, doi:10.1364/OE.24.008967 (2016).

- 34 Warren-Smith, S. C., Nguyen, L. V., Lang, C., Ebendorff-Heidepriem, H. & Monro, T. M. Temperature sensing up to 1300°C using suspended-core microstructured optical fibers. *Optics Express* **24**, 3714-3719, doi:10.1364/OE.24.003714 (2016).
- 35 Warren-Smith, S. *et al.* Stability of Grating-Based Optical Fiber Sensors at High Temperature. *IEEE Sensors Journal* **PP**, 1-1, doi:10.1109/JSEN.2019.2890847 (2019).
- 36 Schartner, E. P. *et al.* Single-peak fiber Bragg gratings in suspended-core optical fibers. *Optics Express* **28**, 23354-23362, doi:10.1364/OE.397537 (2020).
- 37 Hastie, T., Tibshirani, R. & Friedman, J. *The Elements of Statistical Learning*. (Springer New York, 2009).
- 38 Hahnloser, R. H. R., Sarpeshkar, R., Mahowald, M. A., Douglas, R. J. & Seung, H. S. Digital selection and analogue amplification coexist in a cortex-inspired silicon circuit. *Nature* **405**, 947-951, doi:10.1038/35016072 (2000).
- 39 Werbos, P. J. Backpropagation through time: what it does and how to do it. *Proceedings of the IEEE* **78**, 1550-1560, doi:10.1109/5.58337 (1990).

Supplementary information for:

Harnessing the power of complex light propagation in multimode fibers for spatially resolved sensing

Darcy L. Smith^{1,2,3,**}, Linh V. Nguyen^{3,4,**}, Mohammad I. Reja^{1,3}, Erik P. Schartner¹, Heike Ebendorff-Heidepriem¹, David J. Ottaway^{1,2,*} and Stephen C. Warren-Smith^{3,4,*}

¹ *Institute for Photonics and Advanced Sensing and The School of Physics, Chemistry and Earth Sciences, The University of Adelaide, Adelaide, SA 5005, Australia*

² *Australian Research Council Centre of Excellence for Gravitational Wave Discovery (OzGrav)*

³ *Future Industries Institute, University of South Australia, Mawson Lakes, SA 5095, Australia*

⁴ *Laser Physics and Photonics Devices Laboratory, University of South Australia, Mawson Lakes, SA 5095, Australia*

* Correspondence: Stephen C. Warren-Smith (stephen.warren-smith@unisa.edu.au) or David J. Ottaway (david.ottaway@adelaide.edu.au)

** These authors contributed equally to this work.

Fiber characteristics and preparation

Fiber characteristics

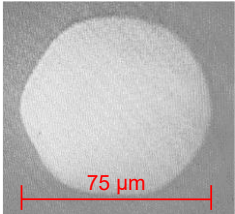
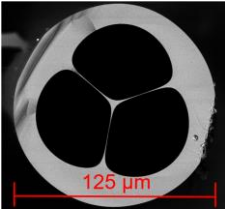
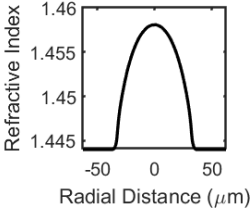
	Sapphire	Suspended-core	Graded-index
Cross section or refractive index profile			
Numerical aperture	1.46	0.2	0.275
Core diameter	70 μm	7 μm	62.5 μm
Approximate number of supported modes	20 000	200	200

Table S1 Comparison of fiber properties. A comparison between the three sensing fibers for a few relevant properties, including cross-sectional image/refractive index profile, the numerical apertures, core diameters and an approximate number of supported modes. The SCF image was taken with a scanning electron microscope, the sapphire fiber image is a screenshot from the camera built into a fiber polisher, and the GRIN fiber refractive index profile was generated from the specified refractive index profile formula.

Properties of the three fibers used for sensing in this experiment are shown in Table **S1**. As mentioned in the Materials and methods section of the main text, the sapphire fiber was manufactured by Micromaterials, the suspended-core fiber (SCF) manufactured in-house¹, and the graded-index (GRIN) fiber manufactured by FS.

Given the high refractive index of crystal sapphire (1.768) and being air-clad, the sapphire fiber supports a high number of modes. However, given the launching conditions (splice from single mode fiber (SMF)), and the sheer number of higher order modes, it is likely that the majority of very high order modes carry negligible power.

Sapphire fiber diameter variation

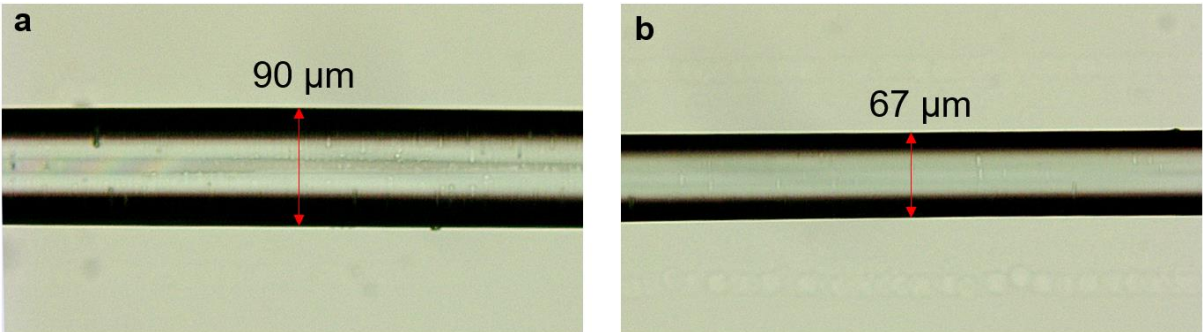


Fig. S1: Sapphire fiber images taken by microscope. **a** and **b** show microscope images approximately 3 mm apart along a length of sapphire fiber.

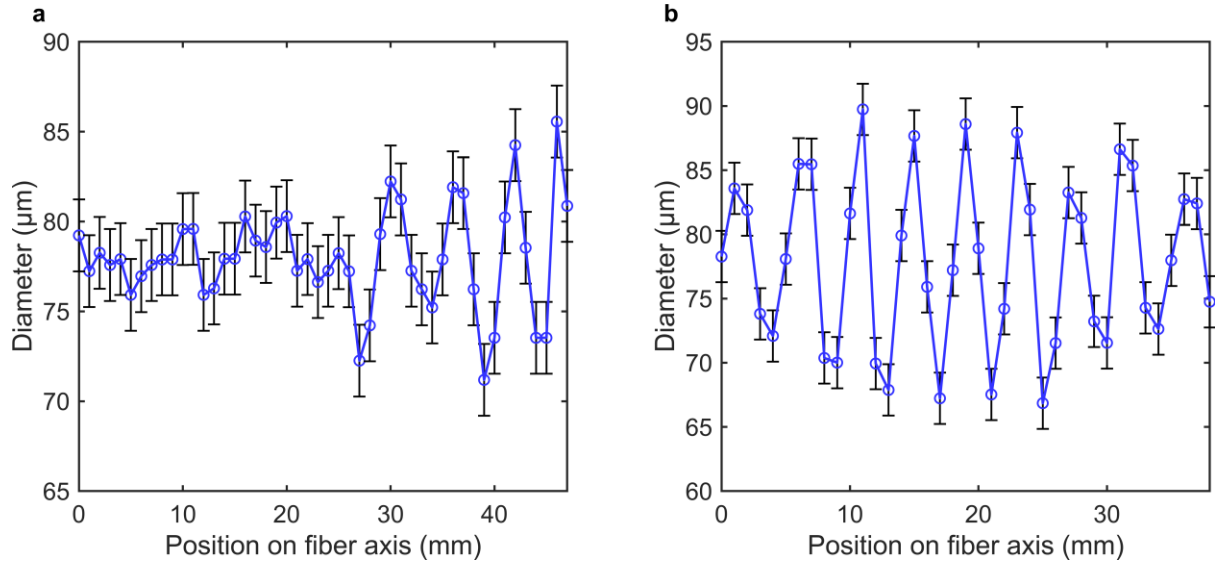


Fig. S2: Variation in sapphire fiber diameter as a function of position. **a** The diameter of an arbitrarily selected ~50 mm length of sapphire fiber as a function of the position along the fiber axis. **b** The diameter of a 40 mm length of sapphire fiber, chosen for its visibly strong variation in diameter, as a function of the position along the fiber axis. The lengths of fiber which generated the plots in **a** and **b** were selected from the same, originally longer length of sapphire fiber, as used in the main experiment.

The light propagating in sapphire fiber experiences considerable mode coupling due to the variation in the fiber's diameter. Both Fig. **S1** and Fig. **S2** highlight this point, the former with microscope images comparing two sections of fiber at opposite ends of the sapphire fiber's diameter range, and the latter with plots of the diameter as a function of position. The length of sapphire fiber used for these measurements was from the same order as the fiber used for sensing in the main experiment. Fig. **S2a** was produced by choosing an arbitrary section of the fiber, while Fig. **S2b** was produced by choosing a section of fiber by inspection with the human eye which appeared to contain stronger diameter variation than the rest of the fiber, so as to demonstrate how strong the variation can be.

Deep learning

Model architectures

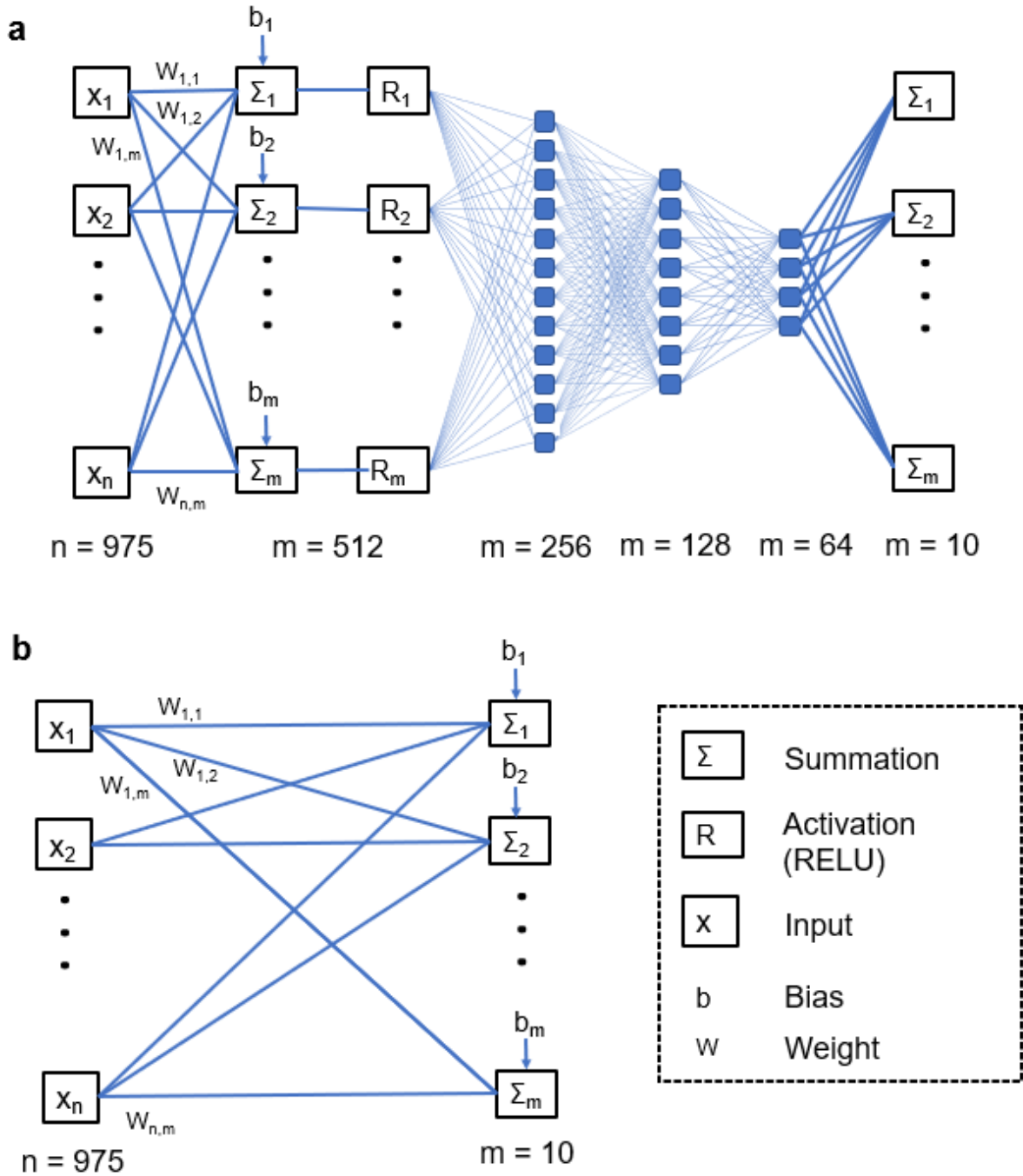


Fig. S3: Schematic of the neural networks. The neural networks trained to map between the 975-point intensity wavelength spectra and 10 temperature labels. **a** The multi-layer perceptron. The general form of a fully-connected DNN layer is shown for the first layer: every node in a layer is a linear combination of every node in the previous layer, with a bias offset. Each node is then passed through a nonlinear activation function, here the rectified linear unit (ReLU) activation function. **b** The linear regressor, which can be thought of as a single, fully-connected layer without the nonlinear activation function. Each node of the output layer is a linear combination of the nodes in the input layer, with a constant bias.

Two neural networks were used to take multimode fiber (MMF) wavelength intensity spectra as input and map to 10-point temperature distributions. The first was a multilayer perceptron

(MLP) with four hidden layers and ReLU nonlinear activation, while the second was a simple linear regressor. Fig. **S3** shows schematics of both, including the general form of a fully-connected layer in an MLP.

Layer type	Output shape	Number of parameters
Input layer	(1,975)	-
Dense hidden layer	(1,512)	499 712
Dense hidden layer	(1,256)	131 328
Dense hidden layer	(1,128)	32 896
Dense hidden layer	(1,64)	8 256
Output layer	(1,10)	650
Total number of trainable parameters		672 842

Table S2 Architecture of the multilayer perceptron. The size and number of trainable parameters of each layer are given.

Layer type	Output shape	Number of parameters
Input layer	(1,975)	-
Output layer	(1,10)	9 760
Total number of trainable parameters		9 760

Table S3 Architecture of the linear regressor. The size and number of trainable parameters of each layer are given.

The neural networks were built using the Keras modular deep learning library for Python². Summaries of the high- and low-capacity models' layers and size are displayed in Table **S2** and Table **S3** respectively. Training was performed on an NVIDIA GeForce RTX 2070 GPU. The 150 epoch long training process took around two hours for the 4-layer model, and around 20 minutes for the 0-layer model.

Backpropagation and stochastic gradient descent was performed using the Adam optimizer³, with a learning rate of 10^{-2} for the linear regressor, and 10^{-3} for the MLP. These values were chosen through brief experimentation as suitably sensitive values for the given architectures.

The training and validation loss as a function of epoch is shown in Fig. **S4**. In none of the cases is underfitting (characterised by lack of convergence) or overfitting (characterised by the simultaneous convergence of the training loss and divergence of the validation loss) present⁴, indicating a suitable selection of architectures and hyperparameters for the given dataset.

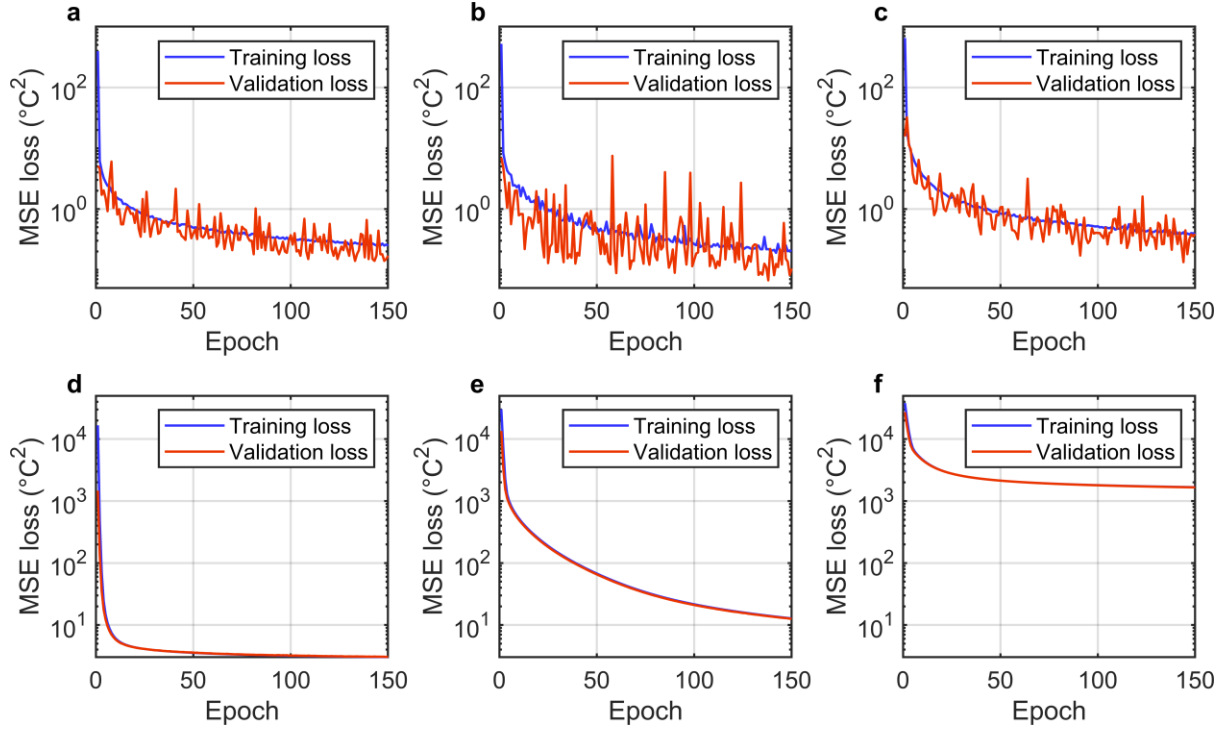


Fig. S4 Deep neural network loss history. **a-c** Training (blue) and validation (red) mean-squared error (MSE) loss as a function of epoch for the MLP trained on the **a** sapphire fiber spectra, **b** SCF spectra and **c** graded index (GRIN) fiber spectra. **d-f** Training and validation mean-squared error loss as a function of epoch for the linear regressor trained on the **d** sapphire fiber spectra, **e** SCF spectra and **f** GRIN spectra. Note the varying x-axis scales in **a-c**, and fixed x-axis scale for **d-f**

Wavelength intensity spectra

Generation of a wavelength intensity spectrum from a specklegram

Consider that Eq. (6) represents the propagation of light through an MMF. Coupling from this MMF into an SMF, and the subsequent propagation of the light, can be represented by multiplying Eq. (6) on the left by $V^{(SMF)} \Lambda^{(SMF)} U^{(SMF)*}$, where $\Lambda^{(SMF)}$ is a 1×1 matrix simply describing the amplitude and phase of the light in the SMF (ignoring polarization). If N eigenmodes are propagating in the K^{th} (final) section of MMF, then $U^{(SMF)*}$ will be a $1 \times N$ matrix representing the projection of these N modes onto the single mode basis. This projection, and consequently the power which will propagate in this single mode, is dependent on the modal power distribution and relative phases of the N modes, which will in turn be dependent on the wavelength of the propagating light. By measuring the intensity output by the SMF at various wavelengths, one obtains a wavelength intensity interference spectrum. Effectively, the information carried by the MMF transmission is projected onto a single value when coupled into the SMF, but one can restore the rich amount of information by scanning this single value across a range of wavelengths, thus transforming the information from the modal to wavelength domain. Further, if the multimode speckle contains

spatially resolved information as a result of mode coupling, then the wavelength spectrum, which is dependent upon the speckle, will also have this information encoded.

Collection and processing of spectra

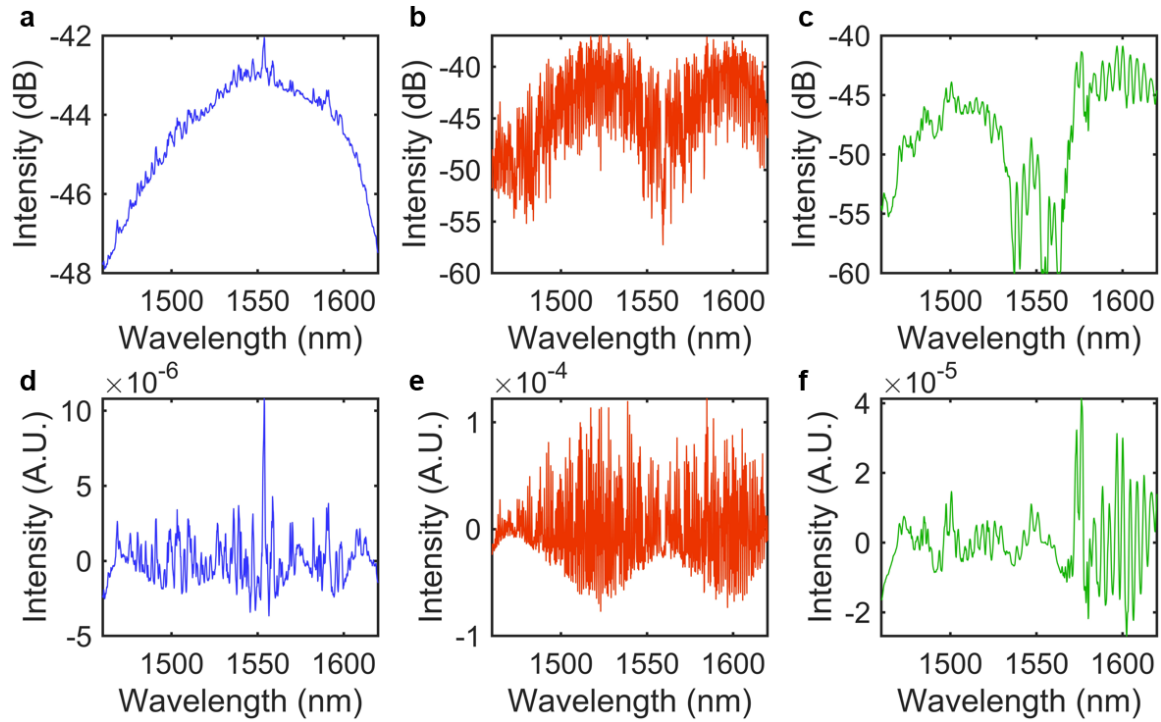


Fig. S5: Wavelength spectra under a uniform room temperature thermal distribution, taken from the **a,d** sapphire fiber, **b,e** the suspended-core fiber and **c,f** the graded-index fiber. **a-c** Raw spectra in a dB scale, as taken directly from the interrogator. **d-f** The same spectra following processing for use in training the deep neural networks. This processing method included two steps; first converting the spectra from a dB to a linear scale, and then removing the five lowest frequency components in their fast Fourier transforms.

The wavelength interference spectra were collected from the fibers using a Hyperion si155 swept source interrogator (Luna Technologies). Examples of spectra exactly as recorded from this interrogator into a .csv format via LabView⁵ are shown in Fig. S5a-c. These spectra existed in the interrogator as 20 000 wavelength points across the 1460-1620 nm range, but were decimated down to 1000 points for computer memory purposes.

All spectra were processed in two major ways. First, they were converted from the dB scale to a linear scale, as per Eq. (S1).

$$I_{lin.} = 10^{\frac{I_{dB}}{10}} \quad (S1)$$

Secondly, the spectra were converted into their fast Fourier transform counterparts, had their five lowest frequency components removed, and had the inverse transform performed. The main motivation for this was to extract the sapphire fiber interference fringes from the strong noise envelope resulting from reflection from the sapphire-silica SMF splice. For consistency, the technique was applied to the spectra from all three fibers.

Sensor fabrication

Sensor assembly

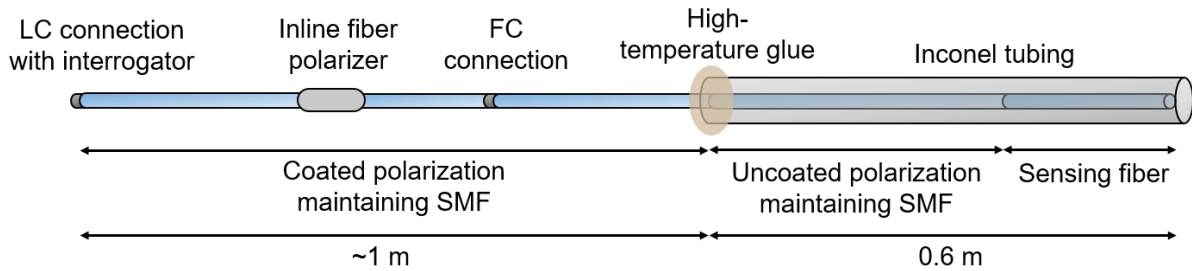


Fig. S6: Dimensions of the sensors. The length of sensing fiber differed for each fiber. These lengths were 0.13 m for the sapphire fiber, 0.24 m for the SCF and 0.29 m for the GRIN.

Each of the three sensors were prepared in the same manner. A schematic of the full sensor is shown in Fig. S6. Each sensor contained two splices: a splice between the sensing fiber and uncoated polarization-maintaining SMF, and a splice between uncoated and coated SMF. An FC connection lay between the sensing fiber and the inline polarizer. The sensor was connected to the interrogator via an LC connection.

The section of SMF within the Inconel tube was stripped of its coating, as this would burn under the high temperature and affect the sensor's output. The fiber was fixed to the Inconel tube with high-temperature glue at the proximal entrance to the tube, thus also sealing the tube. The tube was sealed at the distal end with a crimp.

Splicing

All fiber splicing was performed using a Fujikura FSM-100P fusion arc splicer. Splicing of the SCF and GRIN fibers with the SMF was performed using relatively standard splice settings. The GRIN fiber was manually offset from the SMF transverse to the fiber axes prior to the application of the arc. This was done in order to launch more light towards the edges of the core and attempt to excite more higher order modes. A balance was reached between the offset and the power loss due to the offset splice.

The sapphire fiber required a specially designed splicing program in order to splice to the SMF. An arc from the splicer has no effect on the crystal, hence a program was designed to apply a large arc to the silica SMF, and insert the sapphire facet into the SMF facet while the silica is still malleable. This splicing procedure is inconsistent, and results in high losses even when successful, thus requiring potentially multiple attempts in order to achieve a satisfactory splice. As the sapphire fiber has high loss, its facet at the splice was cut at a non-zero angle and in a non-flat way, so as to prevent reflected light from this facet dominating the recorded spectrum.

Temperature distributions

Localized heating

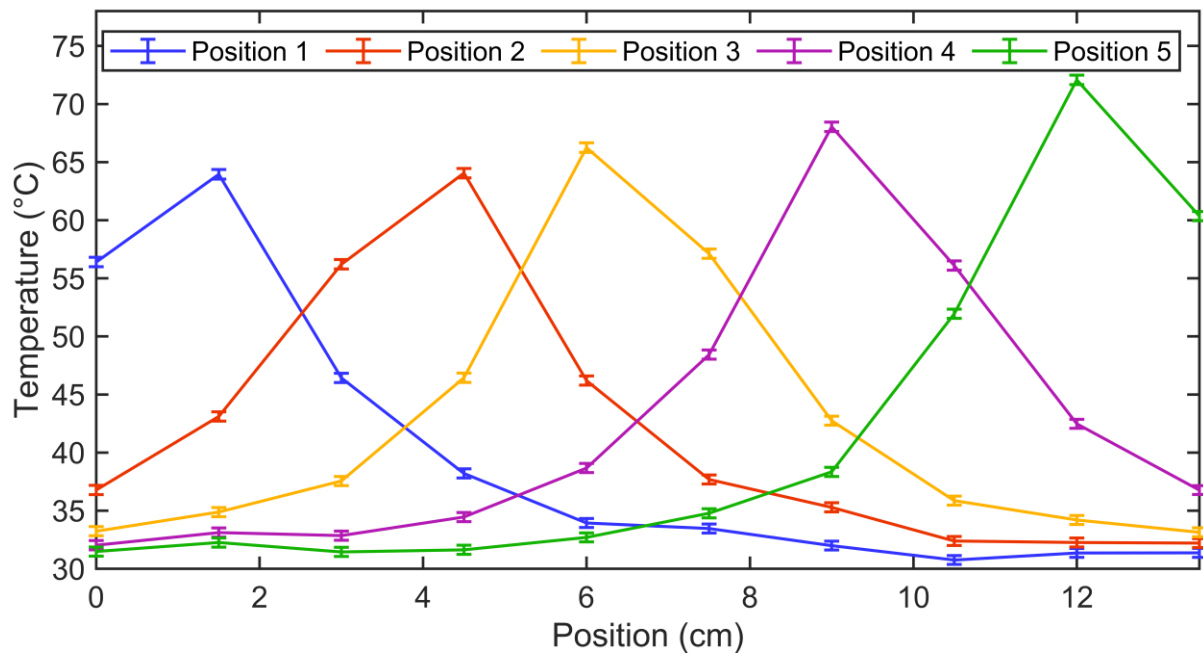


Fig. S7 Heat distributions from the localized heating experiment. Shown are five heat distributions from the five heating positions across the 0.135 m of sensing length which the fibers were subjected to. These temperature measurements were taken using the FBG sensor mentioned in the main text. The fibers were subjected to each heat distribution for 30 mins. The distributions displayed are a single measurement from each 30 mins, but are representative given the stability of each distribution.

For the localized heating experiment, a Peltier heater was used to provide a local heat source to the sensing fibers, which was translated along the sensing fiber axes to provide this heat distribution to five equidistant positions along the fibers. These five temperature distributions are shown in Fig. S7.

Distributed heating

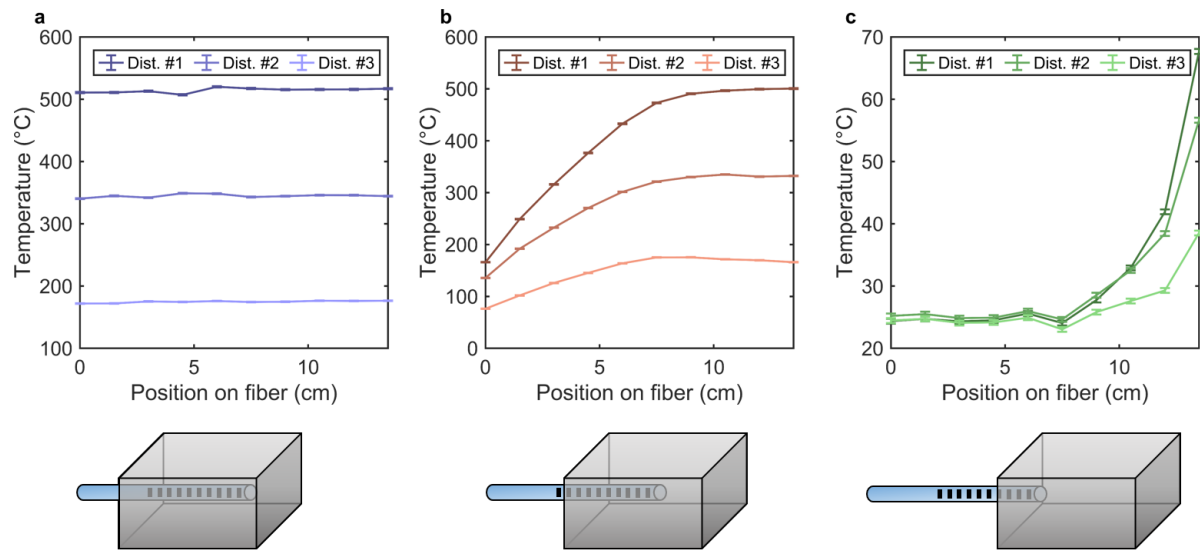


Fig. S8 Heat distributions from the furnace heating experiment. a-c Temperature distributions from three different sensor positions. Seven sensor positions were used to collect spectra from the sensing fibers while the furnace was set to cool from 500°C to room temperature over 20 hours. Within each plot/sensor position, the temperature distributions from three different furnace temperatures are shown. Below are representations of the sensors' and sensing points' position relative to the furnace.

To subject the sensing fibers to various temperature distributions, two dimensions of variation were applied. First, data was collected with the fibers in seven different locations relative to the furnace. This was achieved by simply (manually) translating the fibers along their fiber axis relative to the furnace. Three of these positions are shown in Fig. S8, with Fig. S8a showing distributions from a position where the temperature sensing points were all fully within the furnace, hence the uniform distribution. Fig. S8c shows a sensor position where the sensor was located outside of the furnace, hence only the end of the fibers received a small amount of heat.

For each sensor position, the furnace was left to cool from 500°C to 50°C over a period of 20 h. For each sensor position shown in Fig. S8, three distributions are shown. Distribution #1 is with the furnace at 500°C, and Distributions #2 and #3 progressively further into the furnace's cooling.

Correlation coefficient in the time domain

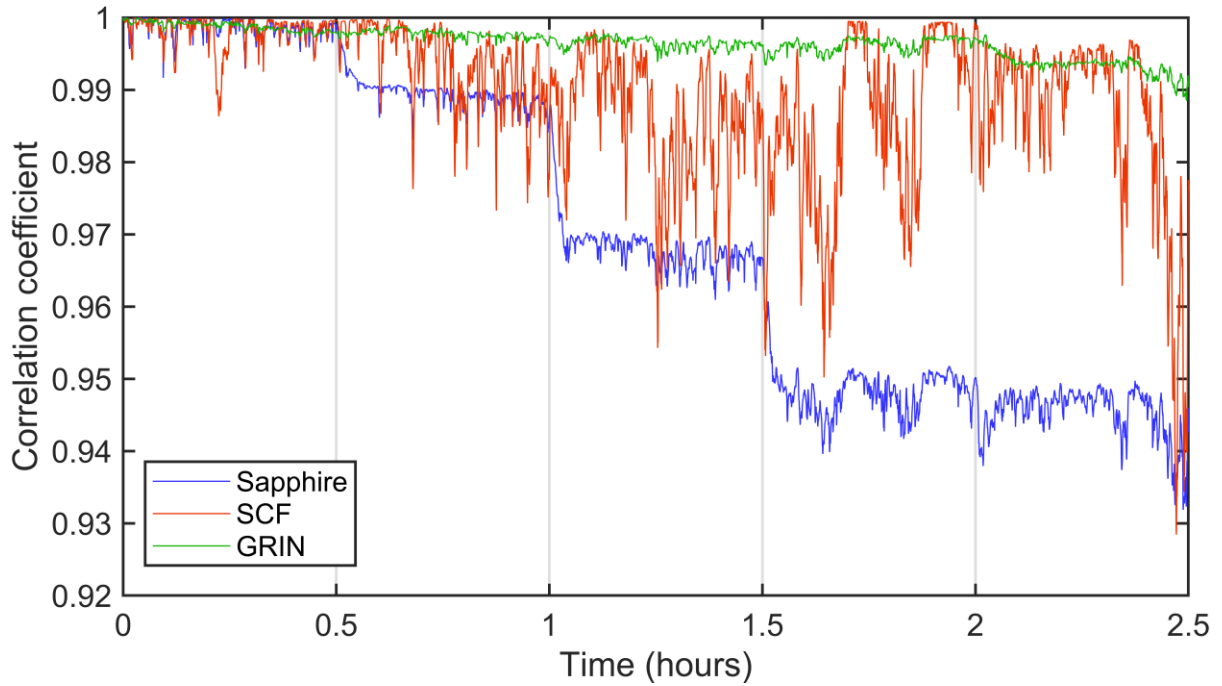


Fig. S9: Temporal change in correlation coefficient. Spectra from the three fibers were collected at a rate of ~ 1 Hz over 2.5 h in order to produce the results seen in Fig 3a, where the correlation coefficient was averaged over each 30 min period and plotted. Shown in this figure is the continuous plotting of the correlation coefficient of each fiber's output in the temporal domain.

Fig 3 in the main text plots the average correlation coefficient of the spectra from each of the fibers over each heating position. Fig. S9 gives the correlation coefficient of the spectra as a function of time, without reducing the correlation coefficient for each heating position to a single average value.

It is clear that in the presence of a certain perturbation, here a local heat source, the sapphire fiber's output is dependent on the position of the perturbation to a much greater extent compared to the SCF and GRIN fiber.

The SCF spectrum is very sensitive to environmental perturbations, leading to an unstable output. This is due to the phase differences between modes of the SCF being highly sensitive to thermal perturbations by design. However, although it is sensitive to the environment, it is relatively insensitive to the position of a perturbation.

Deep learning prediction accuracy per sensing position

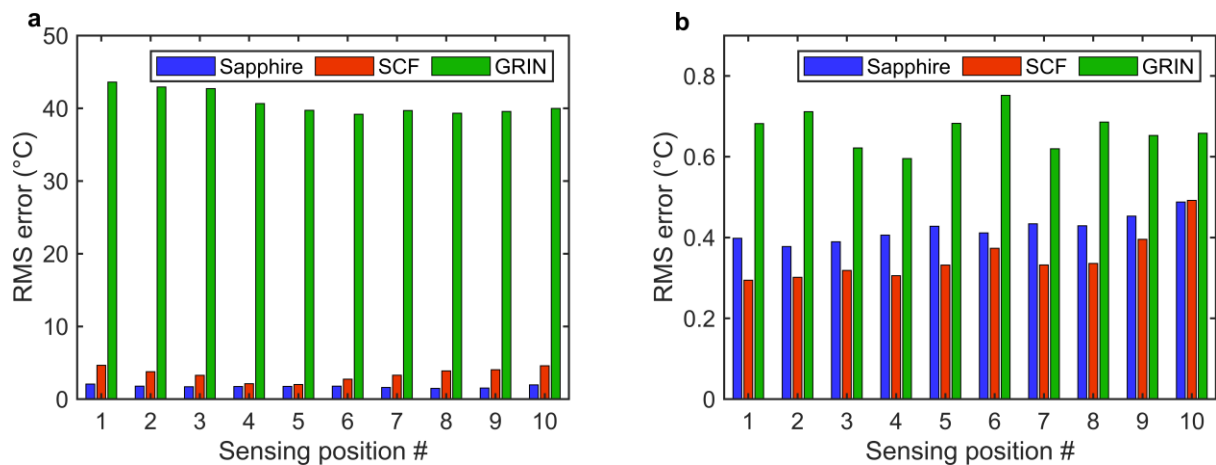


Fig. S10: Deep learning model accuracy for each model and each sensing position. RMS error for predictions made by neural networks on the test set of spectra for the three fibers, by sensing position. **a** Accuracies per sensing position for the linear regressor. **b** Accuracies per sensing position for the multilayer perceptron.

Fig 4 in the main text shows predictions made by the deep learning models trained on spectra from the three fibers. Although the models were trained to predict ten spatially resolved temperature labels per spectrum, the predictions from these ten sensing positions were combined into a single plot for the sake of efficient representation of the results. The accuracy per model per sensing position is shown in Fig. S10 for completeness.

References

- 1 Kostecki, R., Ebendorff-Heidepriem, H., Warren-Smith, S. C. & Monro, T. M. Predicting the drawing conditions for Microstructured Optical Fiber fabrication. *Opt. Mater. Express* **4**, 29-40, doi:10.1364/OME.4.000029 (2014).
- 2 Chollet, F. Keras. (<https://keras.io>, 2015).
- 3 Kingma, D. & Ba, J. Adam: A Method for Stochastic Optimization. *International Conference on Learning Representations*, doi:10.48550/arXiv.1412.6980s (2014).
- 4 Goodfellow, I., Bengio, Y. & Courville, A. *Deep Learning*. (MIT Press, 2016).
- 5 LabVIEW: Advanced programming techniques (CRC Press, 2006).